Using a Discrete Scattering Model to Constrain Water Cloud Model for Simulating Ground-Based Scatterometer Measurements and Retrieving Soil Moisture

Xiaojing Bai, Donghai Zheng, Jun Wen, Xin Wang, and Rogier van der Velde

***Abstract*—Potential of constraining semiempirical model with physically based scatter model simulations has long been recognized. This study contributes to this topic through the assessment of backscattering coefficient (σ^0) simulations and soil moisture retrieval using the water cloud model (WCM) constrained by a discrete scattering model (i.e., Tor Vergata) under both frozen and thawed soil conditions. The WCM is coupled with Oh (hereafter "WCM+Oh") and Dubois (WCM+Dubois) surface scattering models, respectively. The soil permittivity is obtained using the four-phase dielectric mixing model. One year of *C*-band copolarized σ^0 observations are collected by a ground-based scatterometer deployed in the seasonally frozen Tibetan meadow ecosystem. It is found that: the calibrated Tor Vergata (hereafter "TVG") model simulates well the seasonal dynamics and magnitudes of scatterometer measurements, and the simulated scattering components and vegetation transmissivity agree well with the seasonal vegetation dynamics; the total scattering simulated by the TVG constrained WCMs shows a good consistency with the scatterometer measurements, and the simulated soil and vegetation scattering components are in line with the TVG simulations; and the retrieved soil moisture based on the constrained WCMs captures well the seasonal variability noted in the *in situ* measurements. An additional experiment is performed to calibrate the WCMs directly, and the results show that the calibrated WCMs achieve comparable results with the calibrated TVG model and the constrained WCMs in terms of the total σ^0 and soil moisture retrieved. However, the direct calibration of the WCMs leads to unrealistic characterization of individual soil and vegetation scattering contributions, of which an underestimation of the vegetation contribution at VV polarization is most notable. These findings demonstrate that usage of a physically based scatter model to constrain semiempirical models leads to results that provide a more robust representation of reality, which is needed for developing worldwide soil moisture monitoring from active microwave remote sensing.**

***Index Terms*—Active remote sensing, frozen soil, scattering component, Sentinel-1, soil moisture retrieval, Tibetan Plateau, Tor Vergata (TVG) model.**

I. Introduction

AMONG various earth observation technologies, microwave remote sensing is one of the most promising ways for global soil moisture monitoring due to its ability to see through clouds, and to provide also meaningful nighttime data [1]–[3]. Over the past decades, numerous researchers have exerted great efforts for developing soil moisture retrieval algorithms for active microwave remote sensing satellites, including the Advanced Scatterometer (ASCAT) [4], [5], the Aquarius Scatterometer [6], [7], the Soil Moisture Active Passive (SMAP) radar [8], [9], and the Sentinel-1A/B [10]. For example, a time-series-based change detection method developed by Wagner *et al*. [4] and Naeimi *et al*. [5] was used to produce the soil moisture product from the ASCAT observations. However, these studies mainly focused on the thawed soil conditions, and few studies were devoted to simulate backscatter and retrieve soil moisture under frozen soil conditions [11]. In the Northern Hemisphere, more than half of the land surface is covered by permafrost and seasonal frost during winters [12]. Therefore, it is essential to study the microwave scattering characteristics of frozen soil, which is needed to improve the mapping of unfrozen soil water content and the detection of freeze/thaw states.

The most challenging problem is that most of the current soil dielectric mixing models are only applicable to thawed soil conditions, such as the semiempirical models proposed by Wang and Schmugge [13], Dobson *et al*. [14], and Mironov *et al*. [15]. To the best of our knowledge, there are three dielectric mixing models that can be used to estimate the permittivity of frozen soil. One is the four-phase refractive volumetric mixing model originally developed by Birchak *et al*. [16] and used in [17] and [18] to simulate *L*-band emission of frozen soil. Based on the

Manuscript received December 12, 2020; revised June 30, 2021 and August 20, 2021; accepted September 6, 2021. Date of publication September 10, 2021; date of current version September 30, 2021. This work was supported by the National Natural Science Foundation of China under Grant 41801248, Grant 41971308, and Grant 42075065. *(Corresponding author: Donghai Zheng.)*

Xiaojing Bai is with the School of Hydrology and Water Resources, Nanjing University of Information Science and Technology, Nanjing 210044, China (e-mail: xiaojingbai@nuist.edu.cn).

Donghai Zheng is with the National Tibetan Plateau Data Center, State Key Laboratory of Tibetan Plateau Earth System Science, Institute of Tibetan Plateau Research, Chinese Academy of Sciences, Beijing 100101, China (e-mail: zhengd@itpcas.ac.cn).

Jun Wen is with the College of Atmospheric Sciences, Plateau Atmosphere and Environment Key Laboratory of Sichuan Province, Chengdu University of Information Technology, Chengdu 610059, China (e-mail: jwen@cuit.edu.cn).

Xin Wang is with the Key Laboratory of Land Surface Process and Climate Change in Cold and Arid Regions, Northwest Institute of Eco-Environment and Resources, Chinese Academy of Sciences, Lanzhou 730000, China (e-mail: xinwang@lzb.ac.cn).

Rogier van der Velde is with the Faculty of Geo-Information Science and Earth Observation, University of Twente, 7522 Enschede, The Netherlands (e-mail: r.vandervelde@utwente.nl).

Digital Object Identifier 10.1109/JSTARS.2021.3111606

same framework, Zhang *et al*. [19] included the ice component in the dielectric mixing model of Dobson *et al*. [14] for its application to the frozen soil conditions. Recently, Mironov *et al*. [20] developed an improved dielectric mixing model for frozen mineral soils at *L*-band based on their generalized refractive mixing dielectric model [21]. Currently, the performances of these models have been only validated for simulating the brightness temperature (T_b) [17], [22], [23] or retrieving soil moisture at *L*-band [24], [25]. Investigations have not yet studied the performance of the above-mentioned dielectric mixing models in an active microwave remote sensing context.

For simulating the microwave backscatter from vegetation-covered soil surfaces, soil scattering models are often coupled to vegetation scattering models. The commonly used soil scattering models include Oh model [26], [27], Dubois model [28], integral equation model (IEM) [29], and advanced IEM [30], [31], which simulate the backscatter for a variety of surface roughness conditions and sensing configurations. In terms of vegetation scattering models, the water cloud model (WCM) is the most commonly used semiempirical approach to account for the effects of vegetation due to its simplicity and ability to adapt to various land covers [32]. Several vegetation and surface roughness parameters are required by both type of models, which can often be obtained from values reported in scientific literatures, or calibrated based on the satellite and/or ground-based observations. For example, Bindlish and Barros [33] took the ratio of the measured total and IEM soil backscattering coefficient (σ^o) to calibrate the coefficients of the WCM for various land conditions and these calibrated values have been used in other cases [34], [35]. Bai *et al*. [36], [37] used the satellite observations to calibrate the coupled scattering models for simultaneously calibrate the surface roughness parameters and WCM coefficients. Although the calibrated coupled scattering models were proved to be able to simulate well the observed total σ^o, it should be noted that they may fail to simulate individual soil and vegetation scattering components accurately that are important to interpret the microwave signal in relation to the land surface conditions [38], [39]. Therefore, it is imperative to develop a new calibration strategy for these semiempirical scattering models to simulate well both total σ^o and its components.

On the other hand, several investigations have shown the ability of using calibrated physically based scattering models to simulate the temporal variation of satellite observations and retrieve soil moisture. For instance, Dente *et al*. [40] calibrated the discrete scattering model developed at the Tor Vergata University of Rome (hereafter "TVG Model") [41], [42] using both *C*-band ASCAT observed σ^o and AMSR-E observed T_b. The calibrated TVG model was shown to be able to simulate well both active and passive microwave signals over the Tibetan meadow ecosystem. Similar research has been carried out by Wang *et al*. [43], [44] and Bai *et al*. [45] for the same study area using, respectively, Aquarius and SMAP *L*-band active and passive observations. However, these studies are limited to the thawed conditions, whereas the Tibetan Plateau has the largest permafrost area of the world's middle and low latitudes [46], and the freezing period may last about half a year.

Moreover, the numerical complexity of physically based scattering models makes it currently challenging to use them for operational soil moisture mapping applications from a merely computational power perspective. A way to avoid this problem is to use physically based scattering models to provide the parameters of the more efficient semiempirical models. The advantage of this approach is that characteristics of the physically based model are preserved while the computational costs remain low. The traditional calibration methods using the observed total backscatter can find the global optimum model coefficients, but may provide an unrealistic description of individual soil and vegetation scattering contributions. Such models are, thus, unlikely to perform well outside the calibration period. In addition, insufficient observation data sets exist to ensure calibration of those model coefficients for all land covers across the globe.

In this article, we used the calibrated TVG model to constrain the WCM coupled to both the Oh and Dubois soil scattering model for simulating ground-based scatterometer measurements and retrieving soil moisture under both frozen and thawed soil conditions. The four-phase refractive volumetric mixing model is adopted to provide the soil permittivity due to its better performance as suggested by Zheng *et al.* [23]. The analyses are performed using a dataset of concurrent scatterometer and profile soil moisture and soil temperature (SMST) measurements collected at a research site situated in a Tibetan meadow ecosystem. This article is organized as follows. Section II introduces the ground-based scatterometer measurements and other *in situ* measurements. Section III describes the scattering models and methods used to calibrate the model and retrieve soil moisture. Section IV presents the results of the σ^o simulations and soil moisture retrievals. Section V discusses the influence of model calibration strategy on the simulation of total σ^o and its components. Finally, Section VI concludes this article.

II. Materials

A. Field Site and Scatterometer Measurements

The Maqu *in situ* SMST network (see Fig. 1) was established in July 2008 in the source region of Yellow River (SRYR), the northeastern part of the Tibetan Plateau (33°30'-34°15' N-101°38'-102°45'), which is representative for a typical Tibetan meadow ecosystem [47]. The network holds about 20 monitoring stations that continuously measure the SMST at 15-min intervals using 5TM ECH_2O probes installed at soil depths of 5, 10, 20, 40, and 80 cm. For more detailed information on the network, readers are referred to Su *et al*. [47] and Dente *et al*. [48].

At the beginning of 2016, the ELBARA-III radiometer was set up in the center of the SMST network (33.92°N, 102.16°E) [18], [49], and the scatterometer was set up on the same platform in August 2017 (see Fig. 1) [50], which provide the ability for simultaneously observe the land surface using passive and active microwave instruments. The scatterometer system is installed on a 4.8-m-high tower, which is designed using commercially available components and includes a vector network analyzer, four coaxial cables, and two dual-polarization broadband gain horn antennas at a fixed position. The scatterometer measures

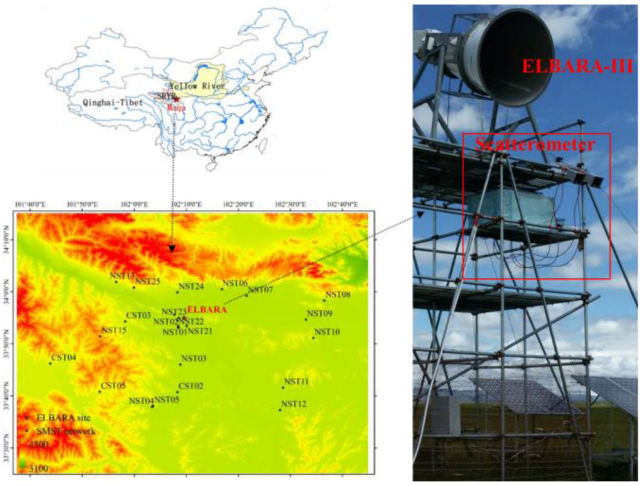

Fig. 1. Location of the scatterometer field site and the Maqu SMST monitoring network in the SRYR. The red box in the right panel indicates the scatterometer observatory system.

the amplitude and phase of the ground surface radar return with a temporal resolution of one- or half-hour over 1–10 GHz in the four linear polarization combinations (VV, HH, HV, VH). The incidence angle is set at 55°. The copolarized σ^o is estimated via a procedure that considers the effects of fading, angular response, and system losses through calibration against reference targets. A detailed description of the observatory system and data processing can be found in [50].

In this article, the copolarized σ^o acquired from August 2017 to August 2018 at 7:00 (hereafter, 7h) and 19:00 (hereafter, 19h) of Beijing Standard Time with specific configuration parameters (*C*-band (4.75 GHz), incidence angle of 55°) is used for the analysis. These two acquisition times correspond to the imaging Sentinel-1A descending and ascending overpasses in this study area. According to Hofste *et al.* [50], the uncertainty in the observed σ^o induced by the effects of fading, calibration, and system stability will not exceed ± 2.5 dB at the *C*-band.

B. Soil and Vegetation Parameters

Concurrent to the scatterometer measurements, SMST profiles are automatically measured adjacent to the scatterometer tower installed at soil depths of 2.5, 5, 7.5, 10, 12.5, 15, 17.5, 20, 25, 30, 35, 40, 45, 50, 60, 70, 80, 90, and 100 cm with Decagon 5TM ECH_2O probes. The soil type of scatterometer field site is sandy loam with on average 2.2% clay, 49.7% sand, and a bulk density of 1.0 g/cm^3 for the surface soil layer. The micrometeorological measurements, including air temperature and solar radiation, are also available. A detailed description of these *in situ* measurements is provided in [18] and [22].

The SMST measured at the top layer of 2.5 cm is used to estimate the soil permittivity using the four-phase dielectric mixing model [16], [18], [25]. The total water content of the soil is equal to the measured liquid water content when the soil is thawed, and is estimated via linear interpolation between the liquid water content measured before and after the freeze-thaw cycle for frozen soil conditions. Leaf area index (LAI) from

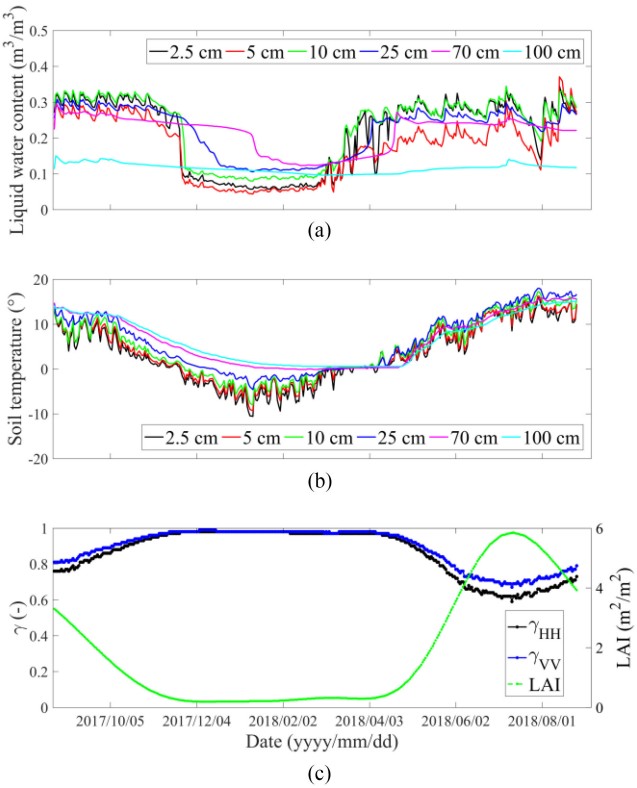

Fig. 2. Time series of (a) soil liquid water content and (b) soil temperature measured at 2.5, 5.0, 10, 25, 70, and 100 cm, and (c) LAI and vegetation transmissivity of HH ($\gamma_{\rm HH}$) and VV polarizations ($\gamma_{\rm VV}$) simulated by the TVG model at 7h.

MODIS product MCD15A3H is used to characterize the vegetation status. The harmonic analysis of the time series algorithm [51] is used to smooth the LAI time series for mitigation of the cloud effects, and a bilinear interpolation method is implemented to match the LAI to the dates of the scatterometer measurements.

Fig. 2(a) and (b) presents the time series of soil liquid water content and soil temperature measured at 2.5, 5, 10, 25, 70, and 100 cm at 7h, respectively. The interpolated LAI derived from the MODIS product is shown in Fig. 2(c), and the scatterometer measured copolarized σ^o is given in Fig. 3. The plots show that the soil is wet and unfrozen with soil temperature larger than 0 °C in the warm season between May and October. During this period, the scatterometer measured copolarized σ^o (black lines in Fig. 3) generally follow the dynamic changes of *in situ* soil moisture at shallow layers, whereby both HH- and VV-polarized σ^o decrease with decreasing soil moisture (e.g., between August and November of 2017), and vice versa (e.g., between April and August of 2018). On the other hand, the surface soil starts freezing since late November with the soil temperature dropping below 0 °C [see Fig. 2(b)]. Followed by the soil freezing, a sharp decrease of soil moisture is observed at the shallow layers, which leads to the rapid decrease in the measured σ^o (see Fig. 3). The frost depth of the soil reaches to its maximum (about 70 cm) in mid of February and later on the soil starts to thaw. With the soil totally thawed at the beginning of April, the soil moisture increases rapidly, resulting in a sharp increase of σ^o. As shown

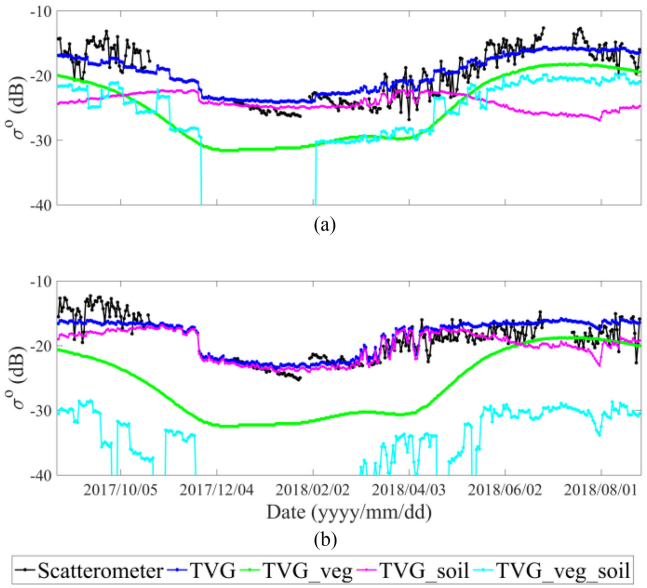

Fig. 3. Time series of scatterometer measurements and TVG simulations at 7h for (a) HH-polarization and (b) VV-polarization. The scatterometer, TVG, TVG_veg, TVG_soil, and TVG_veg_soil stand for the scatterometer measurements, TVG simulated total σ^o and contributions from vegetation, soil, and soil-vegetation interaction, respectively.

in Fig. 2(c), the vegetation starts to grow in May and reaches its growth peak biomass in mid-July, and the senescence process is completed in November.

III. Models and Methods

A. TVG Model

The TVG model is adopted in this study due to extensive validated for the Maqu area [23], [40], [43], [45]. As in [23] and [40], the grass in the Maqu area is characterized by thin dielectric discs with random distribution of orientation, whose scattering cross section and extinction vectors are computed using the Rayleigh–Gans approximation for frequency below 5 GHz [52]. Thickness and radius of the disc are required to compute the scattering and absorption coefficients. The LAI derived from the MODIS product is used to describe the leaf coverage. To compute the vegetation permittivity, Mätzler's vegetation mixing model [53] is used to which the gravimetric moisture content is an input parameter. The soil surface is described as a homogeneous half-space with a rough interface that is simulated by the IEM [29]. The soil moisture, root mean square (rms) height, and correlation length of surface roughness are required to parameterize the IEM. Considering the soil is frozen in the winter, the soil permittivity is calculated with the four-phase dielectric mixing model as in [23] provided in Section II-B. The matrix doubling method [54] is applied twice: once to compute the scattering and transmission matrices of canopy layer and once to resolve the scattering problem for the entire soil-vegetation system. More detailed information on the TVG model can be found in the other scientific contribution, such as [23], [40], [43], and [45].

TABLE I
List of Input Parameters for the TVG Model

Input	Definition	Label	Values	
Sensor	Frequency (GHz)	f	4.75	
	Incidence angle (^{o})	θ	55	
	Soil moisture (m^3/m^3)	mv	*In situ* measurements	
Soil surface	RMS height (cm)	s	0.4	
	Correlation length (cm)	l	7	**Calibration**
	Autocorrelation function	ACF	exponential	Dente *et al.* [40]
Vegetation canopy	LAI (m^2/m^2)	lai	MODIS LAI products	
	Disc radius (cm)	add	1.4	
	Disc thickness (cm)	ldd	0.02	Dente *et al.* [40]
	Disc angular distribution	-	random	
	Plant moisture content (g/g)	$amoidd$	0.4	**Calibration**
Litter	Litter moisture content	$gmoist$	$gmoist = Plitter \times mv$	
			$Plitter = 2$	**Calibration**
	Litter biomass (g/cm^2)	$biomass$	0	

Table I presents the needed input parameters for the TVG model to simulate the scatterometer measurements. The TVG model is adopted to simultaneously simulate the copolarized σ^o at *C*-band (4.75 GHz) with an incidence angle of 55°. The soil moisture is obtained from the *in situ* measurements at 2.5 cm. The surface autocorrelation function is taken as exponential in accordance with previous studies (i.e., [40]). The LAI corresponding to the observation dates of scatterometer is smoothed and interpolated from the MODIS LAI product (see Section II-B). The disc radius, thickness, and angular distribution are adopted from [40], and assumed to be constant during the entire study period. Supported by the previously reported sensitivity analyses on the TVG model [40], [43], [45], the rms height (s), correlation length (l), plant moisture content ($vgwc$), the ratio of litter moisture to soil moisture ($Plitter$), and litter biomass ($Blitter$) are calibrated using the scatterometer measurements.

A look-up table (LUT) method is applied to find an optimum set of input parameters using the following cost function S:

$$S = \frac{\mathrm{MAE}\left(\sigma^o_{\mathrm{HH}}\right)}{\Delta\sigma^o_{\mathrm{HH}}} + \frac{\mathrm{MAE}\left(\sigma^o_{\mathrm{VV}}\right)}{\Delta\sigma^o_{\mathrm{VV}}} \tag{1}$$

where $\mathrm{MAE}(\sigma^o_{pp})$ ($pp = \mathrm{HH}, \mathrm{VV}$) stands for the mean absolute error between the scatterometer measurement and TVG simulation, and $\Delta\sigma^o_{pp}$ indicates the standard deviation in scatterometer measurements.

As part of the LUT calibration procedure, the rms height (s) is varied from 0.1 to 2.0 cm with an increment of 0.1 cm, and the correlation length (l) from 1 to 20 cm with an increment of 1 cm. The plant moisture content ($vgwc$) values from 0.1 to 0.9 g/g with an increment of 0.1 g/g are considered. The litter moisture content is assumed to be linearly related to the soil moisture, with ratio's ($Plitter$) of 0.5, 1.0, 1.5, and 2.0 and the litter biomass ($Blitter$) is varied from 0 to 0.1 g/cm^2 with an increment of 0.02 g/cm^2. This results in a total of 43 200 TVG simulations,

i.e., 20 (s) $\times$10 (l) $\times$ 9 ($vgwc$) $\times$ 4 ($Plitter$) $\times$ 6 ($Blitter$) = 43200. As in [45], the input parameters corresponding to the minimum of S are selected as the optimized parameter set. It should be noted that the optimization process is implemented for the complete study period from August 2017 to August 2018.

B. Soil Scattering Models

The commonly used semiempirical Oh [26], [27] and Dubois soil scattering [28] models are adopted in this study. Based on multifrequency, multipolarization, and multiangular ground-based scatterometer datasets, Oh *et al*. [27] developed an empirical model to quantitatively link the copolarized ratio p and cross-polarized ratio q with the volumetric soil moisture content mv, rms height, correlation length, incidence angle θ, and frequency f. It is described as

$$p = \frac{\sigma^o_{\mathrm{HH,soil}}}{\sigma^o_{\mathrm{VV,soil}}} = 1 - \left(\frac{2\theta}{\pi}\right)^{0.35mv^{-0.65}} e^{-0.4(ks)^{1.4}} \tag{2}$$

$$q = \frac{\sigma^o_{\mathrm{HV,soil}}}{\sigma^o_{\mathrm{VV,soil}}} = 0.1\left(\frac{s}{l} + \sin 1.3\theta\right)^{1.2}\left(1 - e^{-0.9(ks)^{0.8}}\right) \tag{3}$$

$$\sigma^o_{\mathrm{HV,soil}} = 0.11mv^{0.7}\cos^{2.2}\theta\left(1 - e^{-0.32(ks)^{1.8}}\right) \tag{4}$$

where $\sigma^o_{\mathrm{HV,soil}}$, $\sigma^o_{\mathrm{HH,soil}}$, and $\sigma^o_{\mathrm{VV,soil}}$ stand for the bare soil σ^{o} in HV, HH, and VV polarizations, respectively, k is the wave number ($k = 2\pi/\lambda$), λ represents the wavelength ($\lambda = c/f$), and c is the speed of light (3.0×10^8 m/s). The Oh model directly establishes the relationship between the volumetric soil moisture and radar backscatter, which can be performed over a wide range of soil surface conditions, i.e., 0.04 $\mathrm{m^3/m^3} < mv < 0.291$ $\mathrm{m^3/m^3}$, $0.13 < ks < 6.98$, $1.67 < kl < 22.12$, and $10^\circ < \theta < 70^\circ$ [27].

Dubois *et al*. [28] established the relationship between the bare soil copolarized σ^{o} and dielectric constant ε, rms height, incidence angle, and frequency, which are defined as

$$\sigma^o_{\mathrm{HH,soil}} = 10^{-2.75}\left(\frac{\cos^{1.5}\theta}{\sin^5\theta}\right)10^{0.028\varepsilon\tan\theta(ks\sin\theta)^{1.4}\lambda^{0.7}} \tag{5}$$

$$\sigma^o_{\mathrm{VV,soil}} = 10^{-2.35}\left(\frac{\cos^3\theta}{\sin^3\theta}\right)10^{0.046\varepsilon\tan\theta(ks\sin\theta)^{1.1}\lambda^{0.7}}. \tag{6}$$

The roughness parameter involved in the Dubois model is the rms height while the effect of correlation length is neglected. This model was developed under the conditions of $mv < 0.35$ $\mathrm{m^3/m^3}$, $ks < 2.5$, and $\theta > 30^\circ$ [28]. In order to conduct the simulations for both frozen and thawed soil conditions, the quantitative relationship between dielectric constant and soil moisture is defined by the four-phase dielectric mixing model [16], [18], [25]. The soil texture and soil moisture measured at the top layer of 2.5 cm is used as the input.

C. Vegetation Scattering Model

The vegetation and soil scattering models are coupled to simulate the σ^{o} and retrieve soil moisture from the total soil and vegetation system. The semiempirical WCM is frequently used to simulate the vegetation scattering. It assumes the multiple scattering between vegetation and soil can be neglected, and divides the total σ^o_t into vegetation scattering σ^o_{veg} and soil scattering σ^o_{soil} attenuated by the vegetation layer [32]. It is written as follows:

$$\sigma^o_t = \sigma^o_{\mathrm{veg}} + \gamma^2\sigma^o_{\mathrm{soil}} \tag{7}$$

$$\sigma^o_{\mathrm{veg}} = A \times \mathrm{LAI} \times \cos\theta\left(1 - \gamma^2\right) \tag{8}$$

$$\gamma^2 = e^{-2\times B\times \mathrm{LAI}/\cos\theta} \tag{9}$$

where γ^2 stands for the two-way attenuation through the vegetation (-), LAI is a vegetation parameter that accounts for the direct canopy scattering and attenuation ($\mathrm{m^2/m^2}$), and A and B are the model coefficients. The soil σ^{o} in the WCM is computed in this study by the Oh model and Dubois model, respectively. The coupled models are named as WCM+Oh and WCM+Dubois, respectively.

D. Method for Constraining the WCMs

In this article, the TVG model is first optimized using the algorithm described in Section III-A based on the copolarized σ^{o} acquired by the ground-based scatterometer (see Section II-A). Subsequently, the TVG simulations for 19h covering the entire study period are used to estimate the A and B WCM coefficients using the following two cost functions:

$$A = \min\left\{\sum_n\left(\sigma^o_{\mathrm{TVG,veg}} - \sigma^o_{\mathrm{WCM,veg}}\right)\right\} \tag{10}$$

$$B = \min\left\{\sum_n\left(\gamma^2_{\mathrm{TVG}} - \gamma^2_{\mathrm{WCM}}\right)\right\} \tag{11}$$

where n stands for the number of scatterometer observations ($n = 365$). Due to the polarization dependence of the vegetation effects, the values of A and B are derived for the HH and VV polarization separately. The roughness parameters required for the soil scattering models (i.e., Oh and Dubois) are directly parameterized by the optimized values following from the TVG model calibration (see Table I).

Once the WCM coefficients and roughness parameters are determined, the constrained WCMs (i.e., WCM+Oh and WCM+Dubois) are used to simulate the copolarized σ^{o} and validated using the scatterometer measurements. Four error metrics including mean error (Bias), root-mean-square error (RMSE), unbiased RMSE (ubRMSE), and Pearson's correlation coefficient (R) are employed to assess the model performance

$$\mathrm{Bias} = \frac{1}{n}\left(\sum_n \sigma^o_{\mathrm{sim},pp} - \sum_n \sigma^o_{\mathrm{sca},pp}\right) \tag{12}$$

$$\mathrm{RMSE} = \sqrt{\frac{1}{n}\sum_n\left(\sigma^o_{\mathrm{sim},pp} - \sigma^o_{\mathrm{sca},pp}\right)^2} \tag{13}$$

$$\mathrm{ubRMSE} = \sqrt{\mathrm{RMSE}^2 - \mathrm{BIAS}^2} \tag{14}$$

$$R = \frac{\sum_n\left(\sigma^o_{\mathrm{sim},pp} - \bar{\sigma}^o_{\mathrm{sim},pp}\right)\left(\sigma^o_{\mathrm{sca},pp} - \bar{\sigma}^o_{\mathrm{sca},pp}\right)}{\sqrt{\left(\sigma^o_{\mathrm{sim},pp} - \bar{\sigma}^o_{\mathrm{sim},pp}\right)^2}\sqrt{\left(\sigma^o_{\mathrm{sca},pp} - \bar{\sigma}^o_{\mathrm{sca},pp}\right)^2}} \tag{15}$$

where $\sigma^o_{\mathrm{sca},pp}$ and $\sigma^o_{\mathrm{sim},pp}$ (pp = HH, VV) indicate the scatterometer measured and simulated σ^{o} using the WCMs, $\bar{\sigma}^o_{\mathrm{sca},pp}$ and $\bar{\sigma}^o_{\mathrm{sim},pp}$ are their average values, and n stands for the number of data pairs.

E. Soil Moisture Retrieval

Without any further modifications, the constrained WCMs (i.e., WCM+Oh and WCM+Dubois) are used to retrieve soil moisture from the scatterometer measurements. In order to evaluate the suitability of the HH and VV polarizations for retrieving soil moisture, three retrieval schemes are explored: HH-polarized σ^{o} alone (hereafter, SCA-HH), VV-polarized σ^{o} alone (hereafter, SCA-VV), and both HH and VV polarization are used (hereafter, DCA). The following cost functions are formulated:

$$S_{\mathrm{SCA-HH}}\left(mv\right) = \mathrm{RMSE}\left(\sigma^o_{\mathrm{sim,HH}}, \sigma^o_{\mathrm{sca,HH}}\right) \tag{16}$$

$$S_{\mathrm{SCA-VV}}\left(mv\right) = \mathrm{RMSE}\left(\sigma^o_{\mathrm{sim,VV}}, \sigma^o_{\mathrm{sca,VV}}\right) \tag{17}$$

$$S_{\mathrm{DCA}}\left(mv\right) = \frac{1}{2} \left[\mathrm{RMSE}\left(\sigma^o_{\mathrm{sim,HH}}, \sigma^o_{\mathrm{sca,HH}}\right) + \mathrm{RMSE}\left(\sigma^o_{\mathrm{sim,VV}}, \sigma^o_{\mathrm{sca,VV}}\right)\right]. \tag{18}$$

Specifically, an LUT approach is used for the retrievals whereby the soil moisture is varied from 0.01 to 0.35 $\mathrm{m}^3/\mathrm{m}^3$ with increments of 0.002 $\mathrm{m}^3/\mathrm{m}^3$ and the soil moisture value leading to the lowest cost function is considered as the final retrieval. The difference between the minimum and maximum soil moisture is referred to the dynamic range of *in situ* measurements. The Bias, RMSE, ubRMSE, and *R* are used as indicators to evaluate the retrieval accuracy.

IV. Results

A. TVG Simulations

Following the calibration strategy described in Section III-A, five parameters including rms height, correlation length, plant moisture content, ratio of litter moisture content to soil moisture, and litter biomass of the TVG model are optimized using the Scatterometer measurements collected at 19h. Their optimized values are given in Table I. In general, the optimized values are different from those of previous studies focused on large scale using satellite measurements [40], [43], [45]. A zero value of litter biomass is obtained, which is consistent with the optimized results of Zheng *et al*. [55] using both ground-based scatterometer measured *C*-band σ^{o} and ELBARA-III measured *L*-band T_{b}. This result is different from the values reported in [40] using the combination of ASCAT and AMSR-E measurements, which may be caused by the mismatch between footprints of *in situ* and satellite measurements. In addition, the results obtained by Dente *et al*. [40] may have compensated for the effect of topography and roughness heterogeneity that are not considered in the TVG model. Nevertheless, the zero value of litter biomass is also obtained in [40] using only the ASCAT measurements for the calibration. Therefore, additional research is still needed to further investigate the actual contribution of the litter layer and the use of a single model to simulate both active and passive observations. Both are, however, beyond the scope of this research.

TABLE II
Evaluation Metrics Between the Scatterometer Measurements and TVG Simulations

Time	Polarimetric	Evaluation metrics			
		Bias (dB)	RMSE (dB)	ubRMSE (dB)	*R*
19h (Calibration)	HH	-0.50	1.93	1.86	0.89
	VV	0.08	1.90	1.90	0.83
7h (Validation)	HH	0.29	1.96	1.94	0.91
	VV	0.49	1.82	1.75	0.84

The number of simulations for 19h and 7h is 365 and 364, respectively.

Performance of the calibrated TVG model is further assessed by comparing the TVG simulations with ground-based scatterometer measurements collected at 7h. The error metrics including Bias, RMSE, ubRMSE, and *R* are used for the assessment, and listed in Table II for both calibration and validation datasets. The agreements between the scatterometer measurements and TVG simulations lead to *R* values of 0.91 and 0.84 for HH and VV polarizations, respectively. For all the simulations, the RMSE and ubRMSE values are less than 2 dB. From the perspective of error metrics, the TVG simulation results are satisfied compared to previous reported results [40], [43], [45] and the scatterometer measurement accuracy reported in [50].

The scatterometer measured and TVG simulated copolarized σ^{o} at 7h are displayed in Fig. 3, and the scattering components produced by the TVG simulations are shown as well. Data gaps noted in the scatterometer measurements, e.g., in November 2017 and from late June to early July 2018, are mainly caused by power supply failure [50]. The plots illustrate that the calibrated TVG model is able to simulate well both the seasonal dynamics and magnitudes of the scatterometer measurements. As expected, the HH- and VV-polarized σ^{o} decrease in October toward the winter and increase in March for both scatterometer measurements and TVG simulations due to the freezing and thawing of surface soil [see Fig. 2(a)]. For the HH polarization, scattering contributions from vegetation and soil-vegetation interaction dominate the total σ^{o} during the warm season (between May and October), whereas the total σ^{o} is mainly consisted of the soil contribution during cold season (between November and April). The soil scattering generally dominates the total σ° for the VV polarization except during the growing period (in June, July, and August) during which the contributions from vegetation and soil are comparable to each other [see Fig. 3(b)]. Overall, the contributions from vegetation and soil-vegetation interactions are negligible during the cold season [see Fig. 2(b)].

The vegetation transmissivity γ produced by the TVG simulations is also shown in Fig. 2(b), which remains close to 1 during the cold season and gradually decreases with the growth of vegetation. In general, the transmissivity values of both polarizations are comparable to each other with the value of the HH polarization being slightly lower than that of VV polarization.

B. WCMs' Simulations

In terms of WCM, the multiple scattering between vegetation and soil is neglected. As shown in Fig. 3, this assumption is

TABLE III
ROUGHNESS PARAMETERS AND MODEL COEFFICIENTS OF WCM

Models	Roughness parameters		WCMs coefficients			
	s (cm)	l (cm)	A_{HH}	B_{HH}	A_{VV}	B_{VV}
TVG+WCMs	0.4	7	0.009	0.045	0.010	0.034
WCM+Oh	0.6	1	0.475	0.001	0.010	0.001
WCM+Dubois	0.7	-	0.426	0.001	0.001	0.001

The TVG+WCMs stands for the calibration results with TVG. The WCM+Oh and WCM+Dubois stand for the calibration results with the traditional calibration strategy.

TABLE IV
EVALUATION METRICS BETWEEN SCATTEROMETER MEASUREMENTS AND CONSTRAINED OR CALIBRATED WCMS' SIMULATIONS

Time	Polarimetric	Simulation mode	Evaluation metrics			
			Bias (dB)	RMSE (dB)	ubRMSE (dB)	R
19h (Calibration)	HH	WCM+Oh+TVG	-1.44	3.02	2.66	0.79
		WCM+Oh	-0.29	2.31	2.29	0.81
	VV	WCM+Oh+TVG	0.53	2.39	2.33	0.78
		WCM+Oh	0.31	2.16	2.14	0.87
7h (Validation)	HH	WCM+Oh+TVG	-0.55	2.74	2.68	0.84
		WCM+Oh	0.57	2.26	2.19	0.86
	VV	WCM+Oh+TVG	1.13	2.33	2.04	0.80
		WCM+Oh	0.91	2.11	1.91	0.85
19h (Calibration)	HH	WCM+Dubois+TVG	-3.43	3.95	1.96	0.86
		WCM+ Dubois	-0.04	1.89	1.89	0.88
	VV	WCM+Dubois+TVG	-2.23	3.12	2.10	0.76
		WCM+ Dubois	-0.06	1.60	1.60	0.89
7h (Validation)	HH	WCM+Dubois+TVG	-2.60	3.23	1.91	0.89
		WCM+ Dubois	0.80	2.04	1.88	0.90
	VV	WCM+Dubois+TVG	-1.64	2.58	2.00	0.81
		WCM+ Dubois	0.56	1.67	1.58	0.88

reasonable for the study site since the scattering contributions from soil-vegetation interaction simulated by the TVG model are lower compared to soil and vegetation scattering contributions, especially at the VV polarization. The TVG simulated vegetation scattering and transmissivity are used to provide the WCM coefficients A and B using the least square method (see Section III-D). The coefficients (A and B) are separately estimated for the HH and VV polarizations. It should be noted that the WCM coefficients are estimated using the TVG simulations at 19h. The roughness parameters are directly taken from the calibrated values for the TVG model (see Table I), which are given in Table III together with the derived WCM coefficients (i.e., TVG+WCMs). It is found that the derived values for coefficient B for the VV polarization are lower than the ones for the HH polarization due to a higher vegetation transmissivity, and the values of coefficient A are comparable for the two polarizations.

Based on the constrained model coefficients, the WCMs (i.e., WCM+Oh and WCM+Dubois) are used to simulate the scatterometer measurements at 7h. It is worth emphasizing that the four-phase dielectric mixing model [16], [18], [25] is used to compute the soil dielectric constant of surface soil. Table IV presents the error metrics between the scatterometer measurements and the constrained WCMs' simulations. The results demonstrate a better performance of WCM+Oh in comparison to WCM+Dubois in simulating the HH- and VV-polarized σ^o as indicated by lower Bias and RMSE. However, the WCM+Oh simulations perform worse in comparison to the TVG simulations with relatively lower values of R and higher values of RMSE. In addition, the WCM+Oh simulated VV-polarized σ^o agrees better with the scatterometer measurements compared to the HH-polarization.

Figs. 4 and 5 show the scatterometer measured copolarized σ^os (black lines) and simulations (solid blue lines) at

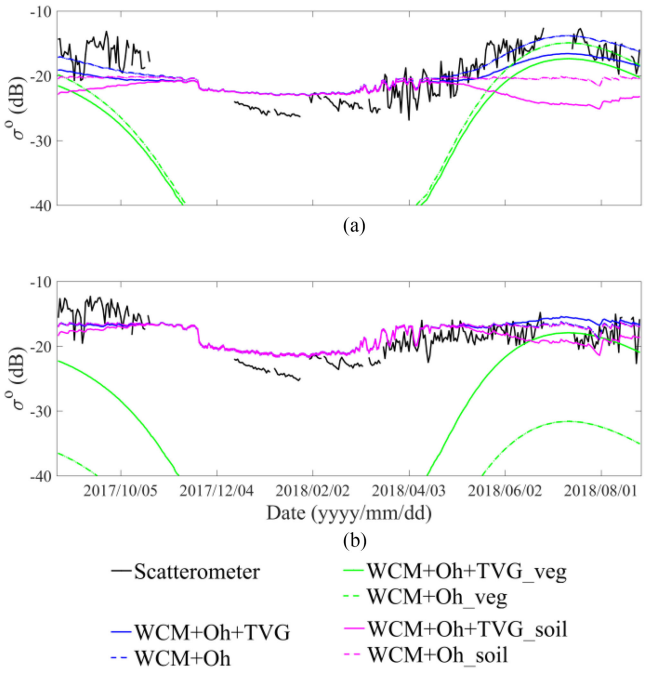

Fig. 4. Time series of scatterometer measurements and WCM+Oh simulations at 7h for (a) HH-polarization and (b) VV-polarization. The Scatterometer stands for the scatterometer measurements. The WCM+Oh+TVG, WCM+Oh+TVG_veg, and WCM+Oh+TVG_soil stand for the total, vegetation, and soil scatterings simulated by the WCM+Oh constrained by the TVG model (solid lines). The WCM+Oh, WCM+Oh _veg, and WCM+Oh _soil stand for the total, vegetation, and soil scatterings simulated by the WCM+Oh calibrated using traditional calibration strategy (dotted lines).

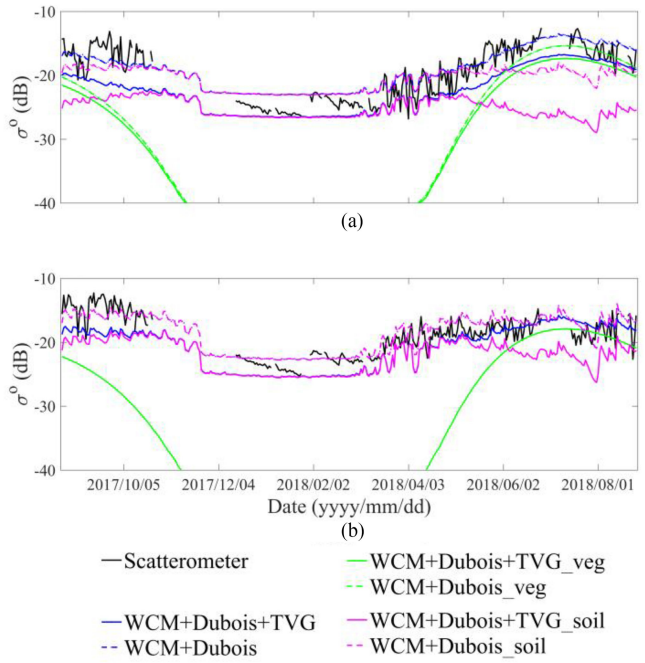

Fig. 5. Time series of scatterometer measurements and WCM+Dubois simulations at 7h for (a) HH-polarization and (b) VV-polarization. The WCM+Dubois+TVG, WCM+Dubois+TVG_veg, and WCM+Dubois+TVG_soil stand for the total, vegetation, and soil scatterings simulated by the WCM+Dubois constrained by the TVG model (solid lines). The WCM+Dubois, WCM+Dubois_veg, and WCM+Dubois_soil stand for the total, vegetation, and soil scatterings simulated by the WCM+Dubois calibrated using traditional calibration strategy (dotted lines).

7h produced by the two constrained WCMs (i.e., WCM+Oh and WCM+Dubois). In addition, vegetation and soil scattering components simulated by the constrained WCMs are shown with solid green and pink lines in the plots, respectively. The figures confirm the overall better performance of the WCM+Oh in simulating the σ^os at both polarizations. The measured HH-polarized σ^o are underestimated by the WCM+Oh [see Fig. 4(a)] during warm season (between May and October) and overestimated during cold season (between November and April). Similarly, the VV-polarized σ^o is also underestimated from August to October and overestimated from November to August by the WCM+Oh simulations [see Fig. 4(b)]. The WCM+Dubois simulations (see Fig. 5) generally underestimate the measured HH- and VV-polarized σ^o year-round.

The simulated vegetation scattering and two-way vegetation transmissivity are almost identical for the two constrained WCMs' simulations (see Figs. 4 and 5). The vegetation scattering generally increases with the growth of grass and becomes the dominant component during the warm season, whereas the contribution is negligible in the cold season. In contrast, the soil scattering is the dominant scattering component during the cold season, whereas its contribution decreases with the growth of grass in the warm season. Regarding the WCM+Oh simulations, the soil scattering estimated for the HH polarization is lower than for the VV polarization (on average of 3.6 dB), whereas the vegetation scattering is almost identical for two polarizations. As a result, the ratio of soil scattering to total scattering is larger in VV polarization compared with that of HH polarization. Similar results can be also noted for the WCM+Dubois simulations.

In comparison to the TVG simulations, the vegetation, soil, and total scatterings simulated by the constrained WCMs generally demonstrate comparable seasonal trends. However, differences can be noted among the magnitude of total scattering and its components simulated by the TVG and constrained WCMs. The vegetation scattering simulated by the two constrained WCMs is almost in line with the simulation results of TVG from June to August 2018, whereas lower values are produced for other months. The soil scattering simulated by the constrained WCM+Oh and WCM+Dubois is comparable to the ones produced by the TVG model for both HH and VV polarizations. In comparison to the TVG simulations, the WCM+Oh overestimates the soil and thus total scattering during the cold season, whereas underestimations are noted in the WCM+Dubois simulations.

In summary, the constrained WCM+Oh model outperforms the constrained WCM+Dubois in simulating total and soil scattering at both polarizations in comparison to the scatterometer measurements as well as the TVG simulations. Furthermore, the WCM+Dubois simulations generally underestimate the scatterometer measurements and TVG simulations.

C. Soil Moisture Retrieval

As shown in [22], the soil moisture retrieved from the *L*-band radiometer observations is in better agreement with the liquid water content measured at 2.5 cm than the one measured at 5.0 cm. Since the penetration depth of *C*-band is shallower than that of the *L*-band [1], it is considered that the soil moisture retrieved from the *C*-band scatterometer measurements best represents the soil water dynamics at surface layer (e.g., $\leq$ 2.5 cm). Therefore, the *in situ* soil moisture at 2.5 cm is taken as a reference for validation of the soil moisture retrievals. The evaluation metrics computed from pairs of *in situ* measurements taken at soil depth of 2.5 cm and soil moisture retrievals based on the above-mentioned two constrained WCMs (see Section III-E) from *C*-band scatterometer measurements at 7h are presented in Table V. The results indicate that significant differences exist between different retrieval methods with *R* values ranging from 0.59 to 0.84 and RMSEs from 0.10 to 0.11 m^3/m^3.

TABLE V
EVALUATION METRICS BETWEEN *IN SITU* MEASUREMENTS OF 2.5 CM AND RETRIEVED SOIL MOISTURE FROM CONSTRAINED OR CALIBRATED WCMS

Polarimetric	Simulation mode	Evaluation metrics			
		Bias (m^3/m^3)	RMSE (m^3/m^3)	ubRMSE (m^3/m^3)	*R*
HH	WCM+Oh+TVG	-0.01	0.09	0.09	0.84
	WCM+Oh	-0.04	0.11	0.10	0.74
VV	WCM+Oh+TVG	-0.07	0.11	0.09	0.70
	WCM+Oh	-0.04	0.08	0.07	0.82
HH+VV	WCM+Oh+TVG	-0.05	0.10	0.10	0.76
	WCM+Oh	-0.04	0.09	0.08	0.81
HH	WCM+Dubois+TVG	0.08	0.10	0.07	0.76
	WCM+ Dubois	-0.05	0.11	0.09	0.77
VV	WCM+Dubois+TVG	0.04	0.10	0.09	0.59
	WCM+ Dubois	-0.02	0.05	0.05	0.91
HH+VV	WCM+Dubois+TVG	0.06	0.10	0.08	0.65
	WCM+ Dubois	-0.03	0.07	0.06	0.89

The number of retrievals at 7h is 364.

For the retrievals based on the constrained WCM+Oh, the implementation of SCA-HH achieves better results compared to the SCA-VV and DCA algorithm as indicated by lower RMSE and higher *R*. Regarding the retrievals produced by the constrained WCM+Dubois, the SCA-VV and DCA provide comparable and better results with respect to the SCA-HH. The SCA-HH retrievals based on the WCM+Oh show better performance compared with those using the WCM+Dubois due to the better performance of WCM+Oh in simulating σ^o at HH polarization (see Section III-B). These results indicate that the accuracy of the soil moisture retrievals is affected by both the adopted soil scattering model and the polarization of the scatterometer measurements.

Overall, the best retrieval result is obtained with the SCA-HH based on the WCM+Oh, which results in RMSE of 0.09 m^3/m^3 and *R* value of 0.84, respectively. This indicates that the better performance of the WCM+Oh in simulating the copolarized σ^o will also lead to better soil moisture retrievals. In general, the error metrics of soil moisture retrievals obtained using the two constrained WCMs in this study are in line with the results reported for the state-of-the-art retrieval algorithm using *C*-band active microwave sensors. For instance, Ma *et al*. [34] found that the matchup of the retrieved soil moisture from Sentinel-1A with measurements in the northeastern Nebraska results in RMSEs ranging from 0.039 to 0.078 m^3/m^3. Also for measurements collected over the vegetated area in the permafrost region of the Tibetan Plateau, Xu *et al*. [56] demonstrated that soil moisture retrievals from Sentinel-1 may yield RMSEs ranging from 0.0308 to 0.094 m^3/m^3.

V. Discussions

In this article, the optimized TVG model is used to constrain the WCMs (i.e., WCM+Oh and WCM+Dubois) for simulating the ground-based scatterometer measurements and retrieving soil moisture. However, the traditional calibration procedure often uses the observation data to calibrate the WCMs directly. The following discussion focuses on the performance assessment of calibrated TVG, constrained WCMs, and calibrated WCMs. For the traditional calibration strategy, the scatterometer measurements collected at 19h during the whole study period are directly used to calibrate the WCMs in this study. Again, the adopted calibration procedure follows the methodology described in [36], whereby the rms height, correlation length, and WCM coefficients A and B at both the HH and VV polarizations are optimized simultaneously. The range of rms height varies from 0.1 to 2.0 cm with increments of 0.1 cm, and correlation length varies from 1 to 20 cm with increments of 1 cm, respectively. The A and B coefficients are optimized within the range between 0.001 and 1.00. The values of rms height, correlation length, A and B, for which the minimum difference between the simulated σ^{o} and scatterometer measurements at 19h are found, are considered as the optimized parameters.

The calibrated roughness parameters and WCMs' coefficients are given in Table III as well. The results are different from the values obtained by constraining the WCMs based on the TVG simulations (see Table III). In general, the traditional calibration strategy using directly the scatterometer measurements tends to produce larger s and lower B values. It should be also noted the optimized B values are all located on the boundary of the domain. On the other hand, the optimized values of s, A, and B for the two coupled WCMs are comparable to each other. The evaluation metrics between scatterometer measurements and calibrated WCMs simulations are given in Table IV as well. In addition, the evaluation metrics between *in situ* and retrieved soil moisture using the calibrated WCMs are given in Table V. From these metrics, it is found that in terms of the total simulated σ^{o} the calibrated WCMs achieve results comparable to the calibrated TVG model and the constrained WCMs. The retrieved soil moisture from the calibrated WCMs is also comparable to those obtained from the constrained WCMs. Furthermore, it should be noted that the values of s and l for the constrained WCMs are directly taken from the calibrated TVG model. Thus, the results of the constrained WCMs may have further improved if also the roughness parameters were calibrated.

The total, vegetation, and soil scattering components simulated by the calibrated WCMs (i.e., WCM+Oh and WCM+Dubois, dotted lines) are also shown in Figs. 4 and 5. In comparison to the simulations produced by the constrained WCM+Oh, the calibrated WCM+Oh tends to produce larger soil scattering during the warm season. Larger vegetation scattering are also obtained for the HH polarization, whereas the vegetation contribution at VV polarization is much smaller especially during the vegetation growth period (between June and August) in comparison to TVG simulations (see Fig. 3). For the simulations of the calibrated WCM+Dubois, much larger soil scattering are obtained across the entire year in comparison to the constrained WCM+Dubois simulations. The weaker vegetation scattering at VV polarization noted for the calibrated WCM+Oh is further amplified (i.e., lower than –40 dB) in the calibrated WCM+Dubois simulations. In general, the vegetation scattering obtained with the calibrated WCMs does not agree with the calibrated TVG simulations as well as previously reported results. For example, Della Vecchia *et al*. [57] showed that the vegetation scattering at the VV polarization dominates the total scattering at high incidence angle of a radar system operating at a low frequency.

In summary, the calibrated WCMs achieve comparable results on the total scattering simulation than the constrained WCMs, but the representation of individual soil and vegetation scattering contributions is unrealistic. For instance, the vegetation scattering at VV polarization produced by the calibrated WCMs is too low based on previous scientific reports and the TVG simulations presented in this manuscript. It should be also noted that the B values obtained for the two calibrated WCMs are located at the edge of the validity parameter domain, which leads to poor results in simulating soil and vegetation contributions. In contrast, the constrained WCMs can rely on the physical scattering processes included in TVG model for providing the model parameters and thereby yield a more realistic simulation of the individual soil and vegetation scattering contributions.

VI. Conclusion

This study explores the potential of using calibrated TVG model to constrain the WCMs (i.e., WCM+Oh and WCM+Dubois) for simulating the copolarized backscatter coefficient (σ^{o}) and retrieving soil moisture for both frozen and thawed soil conditions. A dataset of concurrent scatterometer and profile SMST measurements collected in a Tibetan meadow ecosystem between August 2017 and August 2018 is used for the analysis.

First, the TVG model is calibrated using the scatterometer measurements, which is then used to simulate the total scattering and individual contributions from vegetation, soil, and soil-vegetation pathways. The simulation results show that the calibrated TVG model can correctly simulate the seasonal dynamics and magnitudes of the scatterometer measurements. In addition, the simulated scattering components and vegetation transmissivity comply with the growth of vegetation, whereby the contributions from vegetation and soil-vegetation interaction can be ignored during the cold season due to low vegetation coverage.

Second, the WCMs' coefficients (A and B) are determined using the TVG simulated vegetation scattering and transmissivity based on the least square method, and the needed surface roughness parameter are directly taken from the calibrated TVG model. The results show that the total σ^{o} simulated by the WCMs constrained by the TVG simulations have a good consistency with the scatterometer measurements, and the soil moisture retrievals capture well the seasonal dynamics of *in situ* soil moisture of 2.5 cm. The estimated vegetation and soil scattering contributions agree with the vegetation growth cycle and are comparable to the TVG simulations. Moreover, the constrained WCM+Oh model is found to outperform the WCM+Dubois in simulating σ^{o} and retrieving soil moisture.

Finally, the traditional approach of calibrating the WCM directly on, in this case, the ground-based scatterometer measurements applied for comparison purposes. It is for that the calibrated WCMs achieve comparable results with the calibrated TVG and the constrained WCMs in terms of the total σ^{o}. However, without the constraint of the TVG model, the direct calibration of the WCM results in unrealistic representations of soil and vegetation scattering contribution. Most notably, the vegetation scattering at VV polarization produced by the calibrated WCMs is much smaller.

In conclusion, this study demonstrates the suitability of using the calibrated physically based model (i.e., TVG model) to constrain the semiempirically scattering models (i.e., WCM+Oh and WCM+Dubois) for simulating σ^{o} and retrieving soil moisture. Similar work was previously reported by Acuña *et al*. [58] for airborne *L*-band radar measurements. They also showed that the constrained WCM is able to reproduce well the radar and soil moisture measurements. These positive results encourage to further investigate the combination of physically based and semiempirical models for worldwide backscatter modeling and soil moisture monitoring. In addition, the results presented here are validated by the ground-based scatterometer measurements, and additional work is thus needed to further extend the proposed methodology to satellite applications, such as the Sentinel-1A/B.

REFERENCES

[1] K. C. Kornelsen and P. Coulibaly, "Advances in soil moisture retrieval from synthetic aperture radar and hydrological applications," *J. Hydrol.*, vol. 476, pp. 460–489, 2013.

[2] L. Karthikeyan, M. Pan, N. Wanders, D. N. Kumar, and E. F. Wood, "Four decades of microwave satellite soil moisture observations: Part 1 A review of retrieval algorithms," *Adv. Water Resour.*, vol. 109, pp. 106–120, 2017.

[3] G. P. Petropoulos, G. Ireland, and B. Barrett, "Surface soil moisture retrievals from remote sensing: Current status, products & future trends," *Phys. Chem. Earth*, vol. 83/84, pp. 36–56, 2015.

[4] W. Wagner, G. Lemoine, and H. Rott, "A method for estimating soil moisture from ERS scatterometer and soil data," *Remote Sens. Environ.*, vol. 70, pp. 191−207, 1999.

[5] V. Naeimi, K. Scipal, Z. Bartalis, S. Hasenauer, and W. Wagner, "An improved soil moisture retrieval algorithm for ERS and METOP scatterometer observations," *IEEE Trans. Geosci. Remote Sens.*, vol. 47, no. 7, pp. 1999–2013, Jul. 2009.

[6] Y. Luo *et al.*, "Potential soil moisture products from the aquarius radiometer and scatterometer using an observing system simulation experiment," *Geosci. Instrum. Methods Data Syst.*, vol. 2, no. 1, pp. 113–120. 2013.

[7] K. A. McColl, D. Entekhabi, and M. Piles, "Uncertainty analysis of soil moisture and vegetation indices using Aquarius Scatterometer observations," *IEEE Trans. Geosci. Remote Sens.*, vol. 52, no. 7, pp. 4259–4272, Jul. 2014.

[8] N. N. Das, D. Entekhabi, E. G. Njoku, J. C. Shi, J. T. Johnson, and A. Colliander, "Tests of the SMAP combined radar and radiometer algorithm using airborne field campaign observations and simulated data," *IEEE Trans. Geosci. Remote Sens.*, vol. 52, no. 4, pp. 2018–2028, Apr. 2014.

[9] P. E. O'Neill, S. Chan, E. Njoku, T. J. Jackson, and R. Bindlish, "Algorithm theoretical basis document (ATBD): L2/3_SM_P," Nat. Aeronaut. Space Admin., Jet Propulsion Lab., Pasadena, CA, USA, 2015.

[10] B. Bauer-Marschallinger *et al.*, "Toward global soil moisture monitoring with Sentinel-1: Harnessing assets and overcoming obstacles," *IEEE Trans. Geosci. Remote Sens.*, vol. 57, no. 1, pp. 520–539, Jan. 2019.

[11] X. Xu, C. Derksen, S. H. Yueh, R. S. Dunbar, and A. Colliander, "Freeze/Thaw detection and validation using Aquarius' L-band backscattering data," *IEEE J. Sel. Topics Appl. Earth Observ. Remote Sens.*, vol. 9, no. 4, pp. 1370–1381, Apr. 2016.

[12] T. Zhang, R. G. Barry, K. Knowles, J. A. Heginbottom, and J. Brown, "Statistics and characteristics of permafrost and ground-ice distribution in the Northern Hemisphere," *Polar Geography*, vol. 23, no. 2, pp. 132–154, 1999.

[13] J. R. Wang and T. J. Schmugge, "An empirical model for the complex dielectric permittivity of soil as a function of water content," *IEEE Trans. Geosci. Remote Sens.*, vol. GRS-18, no. 4, pp. 288–295, Oct. 1980.

[14] M. C. Dobson, F. T. Ubaly, M. T. Hallikainen, and M. A. El-Rayes, "Microwave dielectric behavior of wet soil—Part II: Dielectric mixing models," *IEEE Trans. Geosci. Remote Sens.*, vol. GRS-23, no. 1, pp. 35–46, Jan. 1985.

[15] V. Mironov, Y. Kerr, J. P. Wigneron, L. Kosolapova, and F. Demontoux, "Temperature and texture dependent dielectric model for moist soils at 1.4 GHz," *IEEE Geosci. Remote Sens. Lett.*, vol. 10, no. 3, pp. 419–423, May 2013.

[16] J. R. Birchak, C. G. Gardner, J. E. Hipp, and J. M. Victor, "High dielectric constant microwave probes for sensing soil moisture," *Proc. IEEE*, vol. 62, no. 1, pp. 93–98, Jan. 1974.

[17] M. Schwank, M. Stahli, H. Wydler, J. Leuenberger, C. Matzler, and H. Fluhler, "Microwave L-band emission of freezing soil," *IEEE Trans. Geosci. Remote Sens.*, vol. 42, no. 6, pp. 1252–1261, Jun. 2004.

[18] D. Zheng *et al.*, "L-band microwave emission of soil freeze-thaw process in the third pole environment," *IEEE Trans. Geosci. Remote Sens.*, vol. 55, no. 9, pp. 5324–5338, Sep. 2017.

[19] L. Zhang, T. Zhao, L. Jiang, and S. Zhao, "Estimate of phase transition water conten in freeze-thaw process using microwave radiometer," *IEEE Trans. Geosci. Remote Sens.*, vol. 48, no. 12, pp. 4248–4255, Dec. 2010.

[20] V. L. Mironov, L. G. Kosolapova, Y. I. Lukin, A. Y. Karavaysky, and I. P. Molostov, "Temperature and texture dependent dielectric model for frozen and thawed mineral soils at a frequency of 1.4 GHz," *Remote Sens. Environ.*, vol. 200, no. 1, pp. 240–249, 2017.

[21] V. L. Mironov, M. C. Dobson, V. H. Kaupp, S. A. Komarov, and V. N. Kleshchenko, "Generalized refractive mixing dielectric model for moist soils," *IEEE Trans. Geosci. Remote Sens.*, vol. 42, no. 4, pp. 773–785, Apr. 2004.

[22] D. Zheng *et al.*, "Sampling depth of L-band radiometer measurements of soil moisture and freeze-thaw dynamics on the Tibetan Plateau," *Remote Sens. Environ.*, vol. 226, pp. 16–25, 2019.

[23] D. Zheng *et al.*, "Impacts of soil permittivity and temperature profile on L-band microwave emission of frozen soil," *IEEE Trans. Geosci. Remote Sens.*, vol. 59, no. 5, pp. 4080–4093, May 2021.

[24] D. Zheng *et al.*, "Impact of surface roughness, vegetation opacity and soil permittivity on L-band microwave emission and soil moisture retrieval in the third pole environment," *Remote Sens. Environ.*, vol. 209, pp. 633–647, 2018.

[25] D. Zheng *et al.*, "Assessment of soil moisture SMAP retrievals and ELBAR-III measurements in a Tibetan meadow ecosystem," *IEEE Geosci. Remote Sens. Lett.*, vol. 16, no. 9, pp. 1407–1411, Sep. 2019.

[26] Y. Oh, K. Sarabandi, and F. T. Ulaby, "An empirical model and an inversion technique for radar scattering from bare soil surfaces," *IEEE Trans. Geosci. Remote Sens.*, vol. 30, no. 2, pp. 370–381, Mar. 1992.

[27] Y. Oh, K. Sarabandi, and T. T. Ulaby, "Semi-empirical model of the ensemble-averaged differential Mueller matrix for microwave backscattering from bare soil surfaces," *IEEE Trans. Geosci. Remote Sens.*, vol. 40, no. 6, pp. 1348–1355, Jun. 2002.

[28] P. C. Dubois, J. van Zyl, and T. Engman, "Measuring soil moisture with imaging radars," *IEEE Trans. Geosci. Remote Sens.*, vol. 33, no. 4, pp. 915–926, Jul. 1995.

[29] A. K. Fung, *Microwave Scattering and Emission Models and Their Applications*. Norwell, MA, USA: Artech House, 1994.

[30] T. D. Wu, K. S. Chen, J. C. Shi, and A. K. Fung, "A transition model for the reflection coefficients in surface scattering," *IEEE Trans. Geosci. Remote Sens.*, vol. 39, no. 9, pp. 2040–2050, Sep. 2001.

[31] K. S. Chen, T. D. Wu, L. Tsang, Q. Li, J. C. Shi, and A. K. Fung, "Emission of rough surfaces calculated by the integral equation method with comparison to three-dimensional moment method simulations," *IEEE Trans. Geosci. Remote Sens.*, vol. 41, no. 1, pp. 90–101, Jan. 2003.

[32] E. P. W. Attema and F. T. Ulaby, "Vegetation modeled as a water cloud," *Radio Sci.*, vol. 13, pp. 357–364, 1978.

[33] R. Bindlish and P. Barros, "Parameterization of vegetation backscatter in radar-based soil moisture estimation," *Remote Sens. Environ.*, vol. 76, pp. 130–137, 2001.

[34] C. Ma, X. Li, and M. F. McCabe, "Retrieval of high-resolution soil moisture through combination of Sentinel-1 and Sentinel-2 data," *Remote Sens.*, vol. 12, 2020, Art. no. 2303.

[35] A. Sekertekin, A. M Marangoz, and S. Abdikan, "ALOS-2 and Sentinel-1 SAR data sensitivity analysis to surface soil moisture over bare and vegetated agricultural fields," *Comput. Electron. Agriculture*, vol. 171, 2020, Art. no. 105303.

[36] X. Bai *et al.*, "First assessment of Sentinel-1A data for surface soil moisture estimations using a coupled water cloud model and advanced integral equation model over the Tibetan Plateau," *Remote Sens.*, vol. 9, 2017, Art. no. 714.
[37] X. Bai, B. He, and X. Li, "Optimum surface roughness to parameterize advanced integral equation model for soil moisture retrieval in prairie area using Radarsat-2 data," *IEEE Trans. Geosci. Remote Sens.*, vol. 54, no. 4, pp. 2437–2449, Apr. 2016.
[38] S. Hamed Alemohammad, T. Jagdhuber, M. Moghaddam, and D. Entekhabi, "Soil and vegetation scattering contributions in L-band and P-band polarimetric SAR observations," *IEEE Trans. Geosci. Remote Sens.*, vol. 57, no. 11, pp. 8417–8429, Nov. 2019.
[39] A. T. Joseph, R. van der Velde, P. E. O'Neill, R. Lang, and T. Gish, "Effects of corn on C-band and L-band radar backscatter: A correction method for soil moisture retrieval," *Remote Sens. Environ.*, vol. 114, pp. 2417–2430, 2010.
[40] L. Dente, P. Ferrazzoli, Z. Su, R. van der Velde, and L. Guerriero, "Combined use of active and passive microwave satellite data to constrain a discrete scattering model," *Remote Sens. Environ.*, vol. 155, pp. 222–238, 2014.
[41] M. Bracaglia, P. Ferrazzoli, and L. Guerriero, "A fully polarimetric multiple scattering model for crops," *Remote Sens. Environ.*, vol. 54, no. 3, pp. 170–179, 1995.
[42] P. Ferrazzoli and L. Guerriero, "Passive microwave remote sensing of forests: A model investigation," *IEEE Trans. Geosci. Remote Sens.*, vol. 34, no. 2, pp. 433–443, Mar. 1996.
[43] Q. Wang, R. van der Velde, and Z. Su, "Use of a discrete electromagnetic model for simulating aquarius L-band active/passive observations and soil moisture retrieval," *Remote Sens. Environ.*, vol. 205, pp. 434–452, 2018.
[44] Q. Wang, R. van der Velde, P. Ferrazzoli, X. Chen, X. Bai, and Z. Su, "Mapping soil moisture across the Tibetan Plateau plains using aquarius active and passive L-band microwave observations," *Int. J. Appl. Earth Observ. Geoinf.*, vol. 77, pp. 108–118, 2019.
[45] X. Bai *et al.*, "Parameter optimization of a discrete scattering model by integration of global sensitivity analysis using SMAP active and passive observations," *IEEE Trans. Geosci. Remote Sens.*, vol. 57, no. 2, pp. 1084–1099, Feb. 2019.
[46] G. Cheng and H. Jin, "Permafrost and groundwater on the Qinghai-Tibet Plateau and in Northeast China," *Hydrogeol. J.*, vol. 21, no. 1, pp. 5–23, 2013.
[47] Z. Su *et al.*, "The Tibetan Plateau observatory of plateau scale soil moisture and soil temperature (Tibet-Obs) for quantifying uncertainties in coarse resolution satellite and model products," *Hydrol. Earth Syst. Sci.*, vol. 15, pp. 2303–2316, 2011.
[48] L. Dente, Z. Vekerdy, J. Wen, and Z. Su, "Maqu network for validation of satellite-derived soil moisture products," *Int. J. Appl. Earth Observ. Geoinf.*, vol. 17, pp. 55–65, 2012.
[49] Z. Su *et al.*, "Multiyear in-situ L-band microwave radiometry of land surface processes on the Tibetan Plateau," *Sci. Data*, vol. 7, no. 1, pp. 1–3, 2020.
[50] J. G. Hofste *et al.*, "Year-long, broad-band, microwave backscatter observations of an alpine meadow over the Tibetan Plateau with a ground-based scatterometer," *Earth Syst. Sci. Data*, vol. 13, pp. 2819–2856, 2021.
[51] W. Verhoef, M. Menenti, and S. Azzali, "Cover a colour composite of NOAA-AVHRR-NDVI based on time series analysis (1981-1992)," *Int. J. Remote Sens.*, vol. 17, no. 2, pp. 231–235, 1996.
[52] H. J. Eom and A. K. Fung, "A scatter model for vegetation up to Ku band," *Remote Sens. Environ.*, vol. 15, no. 3, pp. 185–200, 1984.
[53] C. Mätzler, "Microwave (1−100 GHz) dielectric model of leaves," *IEEE Trans. Geosci. Remote Sens.*, vol. 32, no. 4, pp. 947–949, Jul. 1994.
[54] H. J. Eom and A. K. Fung, "A scatter model for vegetation up to Ku-band," *Remote Sens. Environ.*, vol. 15, no. 3, pp. 185−200, 1984.
[55] D. Zheng *et al.*, "Active and passive microwave signatures of diurnal soil freeze-thaw transitions on the Tibetan Plateau," *IEEE Trans. Geosci. Remote Sens.*, to be published, doi: 10.1109/TGRS.2021.3092411.
[56] C. Xu, J. J. Qu, X. Hao, and D. Wu, "Monitoring surface soil moisture content over the vegetated area by integrating optical and SAR satellite observations in the permafrost region of Tibetan Plateau," *Remote Sens.*, vol. 12, 2020, Art. no. 183.
[57] A. Della Vecchia, P. Ferrazzoli, L. Guerriero, L. Ninivaggi, T. Strozzi, and U. Wegmüller, "Observating and modeling multifrequency scattering of maize during the whole growth cycle," *IEEE Trans. Geosci. Remote Sens.*, vol. 46, no. 11, pp. 3709–3718, Nov. 2008.
[58] M. A. Acuña, F. Fascetti, P. Ferrazzoli, L. Guerriero, and N. Pierdicca, "Modelling L band backscattering of wheat in Argentinean pampas and its application to soil moisture retrieval," *Int. J. Remote Sens.*, vol. 41, no. 14, pp. 5083–5102, 2020.

Xiaojing Bai received the B.S. degree in electronic information science and technology from Binzhou University, Binzhou, China, in 2010, and the M.S. and Ph.D. degrees in control engineering and information and communication engineer from the University of Electronic Science and Technology of China, Chengdu, China, in 2013 and 2017, respectively.

She is currently a Lecturer with the School of Hydrology and Water Resources, Nanjing University of Information Science and Technology, Nanjing, China. Her current research focuses on soil moisture retrieval from active and passive microwave remote sensing.

Donghai Zheng received the M.A. degree in remote sensing from Beijing Normal University, Beijing, China, in 2010, and the Ph.D. degree in hydrometeorology from the University of Twente, Enschede, The Netherlands, in 2015.

He is currently an Associate Professor with the Institute of Tibetan Plateau Research, Chinese Academy of Sciences, Beijing, China. His main research interests lie in: land surface modeling; soil moisture retrieval using both active and passive microwave measurements; laboratory and *in situ* measurements of soil moisture. His current research focuses on an NSFC project "Retrieval of unfrozen soil water using microwave remote sensing and its application to hydrologic data assimilation over the Tibetan Plateau."

Jun Wen received the B.A. degree from Peking University, Beijing, China, in 1988, the M.A. degree from Lanzhou University, Lanzhou, China, in 1995, and the Ph.D. degree from the Chinese Academy of Sciences, Beijing, China, in 1999, all in meteorology.

He is currently a Professor with the College of Atmospheric Sciences, Chengdu University of Information Technology, Chengdu, China. His research interests include remote sensing and data assimilation, land surface modeling, and climate change.

Xin Wang received the B.A. degree in atmospheric science from Nanjing University, Nanjing, China, in 2007, and the Ph.D. degree in meteorology from the University of Chinese Academy of Sciences, Beijing, China, in 2012.

He is currently an Assistant Professor with the Northwest Institute of Eco-Environment and Resources, Chinese Academy of Sciences, Lanzhou, China. His main research interests lie in: soil moisture and freeze/thaw cycle observation and retrieval using passive microwave measurements in Tibet. His ongoing work focuses on remote sensing land hydrological cycle in Yellow River source catchment with passive microwave both on ground-based and spaceborne radiometer measurements.

Rogier van der Velde received the M.Sc. degree in hydrology from Wageningen University, Wageningen, The Netherlands, in 2004, and the Ph.D. degree in satellite hydrology from the University of Twente, Enschede, The Netherlands, in 2010.

He is currently an Assistant Professor with the Water Resources Department of the Faculty of Geo-Information Science and Earth Observation, University of Twente. His research interests include soil moisture monitoring using both active and passive microwave remote sensing techniques, its validation and application for water resources and agricultural management.